



# A magnetic disturbance index for Mercury's magnetic field derived from MESSENGER Magnetometer data

**Brian J. Anderson**

*The Johns Hopkins University Applied Physics Laboratory, Laurel, Maryland 20723, USA  
(brian.anderson@jhuapl.edu)*

**Catherine L. Johnson**

*Department of Earth and Ocean Sciences, University of British Columbia, Vancouver, British Columbia, Canada  
Planetary Science Institute, Tucson, Arizona, USA*

**Haje Korth**

*The Johns Hopkins University Applied Physics Laboratory, Maryland, USA*

[1] We present a magnetic disturbance measure for Mercury derived from MESSENGER Magnetometer data. Magnetic field fluctuations were computed in three period bands: 0.1–2 s, 2–20 s, and 20–300 s. From these, we determined log average magnetic variability versus latitude and local time in Mercury's magnetosphere. The quietest regions are the southern tail lobe and the nightside poleward of 30° magnetic latitude, and the most disturbed regions are near magnetopause boundaries and the magnetospheric cusp. We used ratios at each location between the mean disturbance and that observed on each pass to compute normalized measures of magnetic disturbance for each orbit. Composite disturbance indices incorporate disturbance levels in all three bands. Percentile ranking of the composite indices provides a quantitative basis for selecting data from quiet to disturbed conditions.

**Components:** 7,760 words, 8 figures, 4 tables.

**Keywords:** Mercury; magnetic field; magnetosphere; disturbance index.

**Index Terms:** 2756 Planetary magnetospheres: Magnetospheric physics; 5737 Magnetospheres: Planetary sciences: Fluid planets; 6033 Magnetospheres: Planetary sciences: comets and small bodies; 5440 Magnetic fields and magnetism: Planetary sciences: Solid surface planets; 5443 Magnetospheres: Planetary sciences: Solid surface planets; 6235 Mercury: Planetary sciences: Solar system objects; 0520 Data analysis: algorithms and implementation: Computational geophysics.

**Received** 24 April 2013; **Revised** 22 July 2013; **Accepted** 5 August 2013; **Published** 23 September 2013.

Anderson, B. J., C. L. Johnson, and H. Korth (2013), A magnetic disturbance index for Mercury's magnetic field derived from MESSENGER Magnetometer data, *Geochem. Geophys. Geosyst.*, 14, 3875–3886, doi:10.1002/ggge.20242

## 1. Introduction

[2] The discovery of Mercury's magnetic field by *Ness et al.* [1974, 1975] presented a challenge to

theories of planetary magnetic field generation because the dipole moment is too large to be a remanent field and too small to result from a conventional dynamo [Solomon, 1976; Srnka, 1976;



Jackson and Beard, 1977; Stevenson *et al.*, 1983; Connerney and Ness, 1988]. Analyses of observations from both Mariner 10 and M<sup>E</sup>rcury Surface, Space ENvironment, GEOchemistry, and Ranging (MESSENGER) spacecraft flybys confirmed these results [Anderson *et al.*, 2008, 2010; Uno *et al.*, 2009]. MESSENGER data acquired from orbit about Mercury indicate a planetary moment of  $190 \text{ nT-R}_M^3$  [Johnson *et al.*, 2012] that is offset to the north by 479 km and aligned with the planetary spin axis to within  $1^\circ$  [Anderson *et al.*, 2011, 2012].

[3] These results may favor models of Mercury's core similar to those proposed for Saturn [Stevenson, 1982] that invoke a nonconvecting layer over a deep dynamo [Christensen, 2006; Christensen and Wicht, 2008]. Whether this model can yield a field without higher-order structure is not clear [Stanley and Mohammadi, 2008; Manglik *et al.*, 2010]. The MESSENGER orbit at Mercury implies that structure in the southern hemisphere may be evident only in subtle signatures in the MESSENGER data [Korth *et al.*, 2004; Richer *et al.*, 2012]. Analyses of MESSENGER orbital data indicate that departures from the offset dipole in the spherical harmonic Gauss coefficients  $g_{30}$  and  $g_{40}$  are smaller than  $\sim 7\%$  of the dipole term,  $g_{10}$  [Anderson *et al.*, 2012].

[4] The importance of higher-order structure makes it critical to identify data that give the clearest measures of the intrinsic field. The small planetary moment and Mercury's proximity to the Sun imply that the externally and internally generated fields can be comparable [Korth *et al.*, 2004; Slavin *et al.*, 2007; Anderson *et al.*, 2010], and both must be treated in solutions for the intrinsic field [Johnson *et al.*, 2012]. The external magnetic field is also dynamic [Slavin *et al.*, 2008, 2009, 2010a, 2010b, 2012a, 2012b; Sundberg *et al.*, 2010, 2012a, 2012b; Korth *et al.*, 2011, 2012; DiBraccio *et al.*, 2013]. This paper defines a magnetic disturbance index for Mercury to identify data that are relatively free of external field dynamics and to provide a measure of magnetospheric activity for studies of the external field.

## 2. Challenges

### 2.1. General Considerations

[5] At Earth, magnetic indices are derived from ground-based magnetometer observations [cf. Mayaud, 1980]. At Mercury, only data from orbit are available. The solar-wind-magnetosphere interaction at Earth is particularly sensitive to the north-

south component of the interplanetary magnetic field (IMF),  $B_{z\text{-IMF}}$ , but  $B_{z\text{-IMF}}$  cannot be usefully constrained at Mercury with MESSENGER data. The magnetospheric convection timescale is much shorter than the time it takes MESSENGER to transit the magnetosphere [e.g., Slavin *et al.*, 2007]. Moreover,  $B_{z\text{-IMF}}$  measured before and after magnetosphere passes are uncorrelated [Winslow *et al.*, 2012], indicating that MESSENGER solar wind data do not provide a measure of  $B_{z\text{-IMF}}$  during magnetosphere transits. Thus, data within the magnetosphere must be used to assess the disturbance level. Indicators of dynamics include reconnection signatures at the magnetotail and magnetopause [Slavin *et al.*, 2009, 2010a, 2010b, 2012a, 2012b; Sundberg *et al.*, 2012a; DiBraccio *et al.*, 2013], magnetopause boundary waves [Boardsen *et al.*, 2010; Sundberg *et al.*, 2010, 2012b], and diamagnetic field depressions in the plasma sheet and northern cusp [Korth *et al.*, 2011, 2012; Winslow *et al.*, 2012]. Because the convection timescale for Mercury is  $\sim 2$  min [Russell *et al.*, 1988; Glassmeier *et al.*, 1997; Slavin *et al.*, 2007], the absence of magnetopause or tail reconnection signatures when the spacecraft passes through these regions is no guarantee that reconnection was not occurring at other times during the pass. The disturbance measure should thus consider the relative fluctuation levels throughout the orbit.

### 2.2. Processes and Timescales

[6] Period bands for the assessment of magnetic disturbance were chosen on the basis of characteristics of known or predicted physical processes (Table 1). The MESSENGER Magnetometer [Anderson *et al.*, 2007] was operated at its maximum rate, 20 vector samples/s, through magnetospheric transits. The relevant timescales for magnetospheric processes at Mercury range from the convection timescale of  $\sim 2$  min [Russell *et al.*, 1988; Slavin *et al.*, 2007] to ion plasma wave frequencies of several hertz [Russell, 1989; Glassmeier, 1997; Glassmeier *et al.*, 2003; Trávníček *et al.*, 2009; Boardsen *et al.*, 2009, 2012]. We identified three period ranges: 0.1–2 s; 2–20 s; and 20–300 s, corresponding approximately to the physical phenomena as listed in Table 1.

### 2.3. Considerations for Mercury and MESSENGER's Orbit

[7] The MESSENGER spacecraft [Solomon *et al.*, 2007] entered orbit about Mercury on 18 March 2011 with 200 km periapsis and 15,300 km apoapsis altitudes,  $82.5^\circ$  inclination, and 12 h period. On



**Table 1.** Period Bands Used for Computing Magnetic Fluctuation Levels and Corresponding Physical Processes that have Magnetic Signals in Mercury’s Magnetosphere

Period Band (s)	Physical Processes <sup>a</sup>
1: 0.1–2.0	Proton instabilities [Glassmeier et al., 2003; Trávníček et al., 2009; Boardsen et al., 2009, 2012] Flux ropes [Slavin et al., 2008, 2009, 2012b] Small-scale plasma structures and turbulence [Trávníček et al., 2009] <sup>b</sup>
2: 2–20	Flux transfer events [Slavin et al., 2010a, 2012b; DiBraccio et al., 2013] Traveling compression regions [Slavin et al., 2009, 2012b] Kelvin-Helmholtz waves [Boardsen et al., 2010; Sundberg et al., 2010, 2012b] Heavy-ion instabilities [Glassmeier, 1997; Ip, 1987] Fast-mode wave transit time [Russell, 1989; Glassmeier et al., 2003]
3: 20–300	Diamagnetic plasma pressure depressions in the cusp and plasma sheet [Korth et al., 2011, 2012; Winslow et al., 2012] <sup>c</sup> Global convection dynamics [Russell et al., 1988; Glassmeier, 1997; Slavin et al., 2007, 2010b; Sundberg et al., 2012a]

<sup>a</sup>Processes are listed in the period range at which their signals are predominantly observed or predicted, given that most physical processes generate signals in adjacent period bands.

<sup>b</sup>Not all possible physical processes are listed, and some of those listed have been predicted but have not yet been confirmed observationally.

<sup>c</sup>The time scales of magnetic signatures due to plasma depressions in the cusp and plasma sheet depend on the spacecraft orbit geometry and fall in this period range for the MESSENGER orbit.

16 March 2012, the orbit period was reduced to 8 h [McAdams et al., 2012]. For simplicity, we here consider data only through 15 March 2012. Figure 1 shows the MESSENGER orbit in Mercury solar orbital (MSO) coordinates for three passes, two in the so-called short-eclipse season (Figures 1a and 1b), inbound on the dayside, and one in the long-eclipse season, inbound on the nightside (Figure 1c). The MSO origin is the center of Mercury, with the  $X$ -axis positive sunward, the  $Z$ -axis parallel to the planetary rotation axis, positive northward, and the  $Y$ -axis completing a right-handed system. As Mercury orbits the Sun, the MESSENGER orbit sweeps through local time westward so that local-time sampling is synchronized with heliocentric distance [cf. Pettengill and Dyce, 1965; Colombo, 1965; McAdams et al., 2007].

### 3. Input Data and Initial Processing

#### 3.1. Coordinate Systems

[8] We used the MSO system and Mercury solar magnetospheric (MSM) coordinate system for this analysis. The MSM directions are the same as MSO, but the origin is centered on the planetary

dipole, offset 479 km northward along the planetary spin axis [Anderson et al., 2012]. We aberrated the systems using an average radial solar wind speed of 400 km/s and Mercury’s orbital velocity so that aberrated positive  $X$  is opposite the solar wind flow in Mercury’s frame [Johnson et al., 2012]. In either aberrated system, we denote the spacecraft position as  $\mathbf{r} = (X, Y, Z)$  and magnetic field data as  $\mathbf{B} = (B_X, B_Y, B_Z)$ . Latitude,  $\lambda$ , longitude,  $\phi$ , and local time,  $h$ , are given by

$$\lambda = \sin^{-1}(Z/r) \quad (1a)$$

$$\phi = \tan^{-1}(Y, X) \quad (1b)$$

$$h = 12 \bmod (\phi/\pi + 1, 2) \quad (1c)$$

where  $r = |\mathbf{r}|$ ,  $h$  is in hours, and the mod operator returns the remainder after dividing the first argument by the second.

[9] For periods longer than a few seconds, the variation of the field along the spacecraft trajectory is substantial, so the internal dipole field,  $\mathbf{B}_{\text{Int}}$ , was subtracted

$$\delta\mathbf{B} = \mathbf{B} - \mathbf{B}_{\text{Int}}(\mathbf{r}) \quad (2)$$

[10] We did not subtract an estimate for the external field because it varies gradually with position.

#### 3.2. Example Magnetic Fluctuations

[11] Two magnetosphere passes are shown in Figures 2 and 3. For the first case (Figure 2), from 07:32 to ~07:42 UTC, the field magnitude and component values changed by tens of nT in less than a minute, and the spectral power from 0.1 to 10 Hz was much greater than near periapsis. The field varied more smoothly through periapsis, from 07:50 to 07:55 UTC. Pure tones near 0.7 Hz and 2 Hz are due to small ( $<1^\circ$  amplitude) oscillations of the Magnetometer boom (most evident near periapsis where the field is strongest). Near 08:04 UTC,  $B_X$  reversed sign, indicating the magnetic equator. As the spacecraft approached the current sheet, the field variability and power from 0.1 to 10 Hz increased. From 08:04 to 08:08 UTC, there were narrow-band emissions indicating ion-plasma waves [cf. Boardsen et al., 2012]. Thereafter, until just prior to the outbound magnetopause crossing, fluctuation levels were ~5 nT (amplitude) and there were broadband emissions from 0.1 to 10 Hz. Increases in the field magnitude near 08:10 and 08:14 UTC are consistent with substorm dipolarizations [cf. Sundberg et al.,

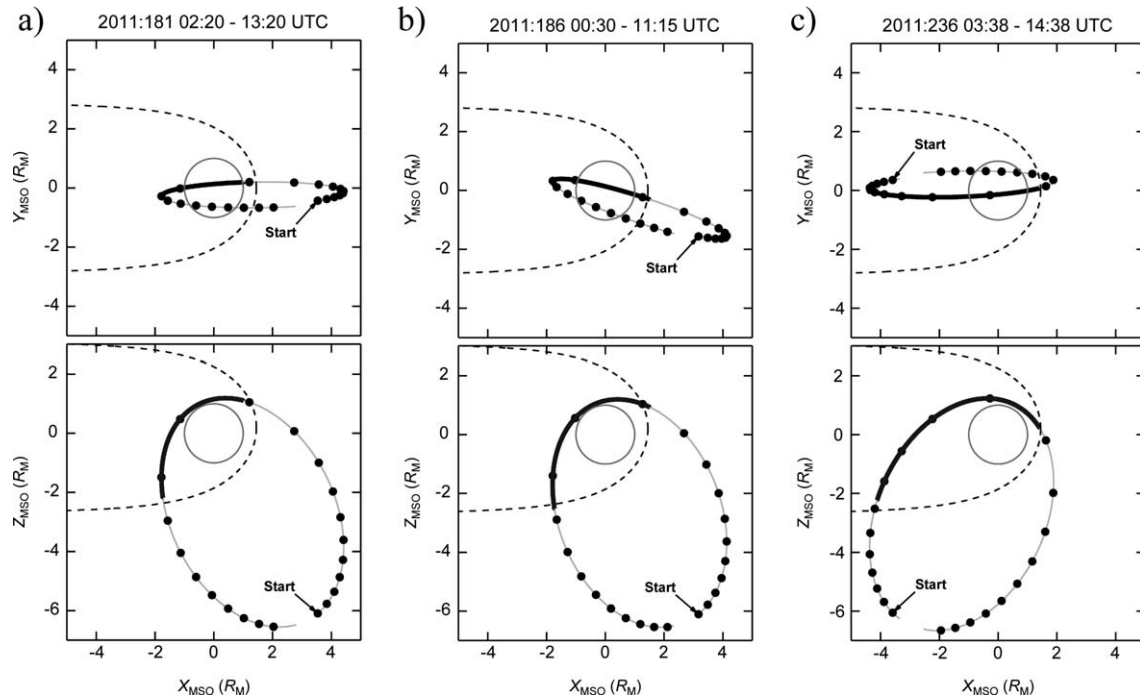


**Figure 1.** MESSANGER spacecraft trajectory (gray traces) for the first magnetospheric transits on day 181 (left), day 186 (middle), and day 236 (right) of 2011 plotted as projections in the  $Y$ - $X$  MSO plane (top) and  $Z$ - $X$  MSO plane (bottom). Heavy black lines indicate the magnetospheric transit. Black dots are plotted every 30 minutes starting at 02:30 UTC (left), 00:30 UTC (middle), and 04:00 UTC (right). Arrows indicate the start of the orbit segment. The average magnetopause fit intersecting each plane is shown by the dashed traces, and the dark brown circles denote outlines of Mercury's surface. The Sun is to the right for all panels.

2012a]. The outbound magnetopause crossing occurred just after 08:43 UTC.

[12] For the second case (Figure 3), the inbound magnetopause crossing occurred at 05:26 UTC. Enhanced fluctuations and broadband power are evident until 05:30 UTC but at lower levels than in Figure 2. Some  $\sim 5$  nT fluctuations and 0.1 to 1 Hz emissions persisted until  $\sim 05:42$  UTC. From 05:42 to 05:59 UTC, the field varied smoothly and the emission power over 0.1–10 Hz was low. The magnetic equator was observed near 06:05 UTC, and broadband emissions occurred from 05:59 to 06:09 UTC, spanning the magnetic equator. The spacecraft remained in the southern magnetic lobe (negative  $B_X$ ) from 0609 to 0643 UTC, and the field was quiet. Broadband emissions intensified at 06:52 UTC as the spacecraft approached the magnetopause.

### 3.3. Passband Filtering and Standard Deviations

[13] Reduced data records available for MESSANGER Magnetometer observations include 1-s averages,  $\langle \delta \mathbf{B} \rangle$ , and standard deviations for each field component. We used data between the innermost

inbound and outbound magnetopause crossings, as documented by Winslow *et al.* [2013]. The standard deviations of each component are denoted  $\sigma_{NX}$ ,  $\sigma_{NY}$ , and  $\sigma_{NZ}$ , respectively where  $N = 1, 2, \text{ or } 3$  is the period band (Table 1). The net fluctuation is defined as

$$\sigma_N = \sqrt{\sigma_{NX}^2 + \sigma_{NY}^2 + \sigma_{NZ}^2} \quad (3)$$

[14] The responses of  $\sigma_1$ ,  $\sigma_2$ , and  $\sigma_3$  with period are shown in Figure 4. The oscillatory response of  $\sigma_1$  is characteristic of a simple box-car average [Bloomfield, 2000]. The 50% attenuation level of the 1-s averages occurs at 2 s period.

[15] For  $\sigma_2$  and  $\sigma_3$ , we applied a three-pass box-car average using different time windows to optimize the period response functions. For  $\sigma_2$ , we used 5-point, 7-point, and 9-point averages. This three-pass average gives 50% attenuation at 21.0 s period. Denoting these averages as  $\langle \delta \mathbf{B} \rangle_{20}$ , the passband for 2 to 20 s is given by

$$\delta \mathbf{B}_2 = \langle \delta \mathbf{B} \rangle - \langle \delta \mathbf{B} \rangle_{20} \quad (4)$$

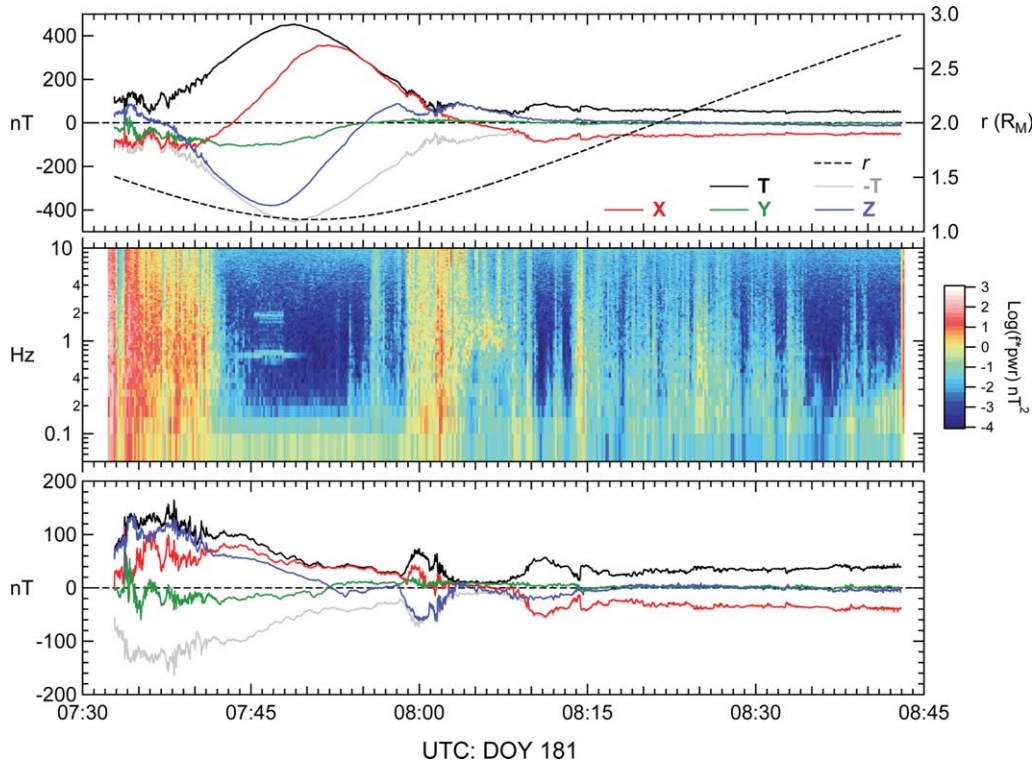


**Figure 2.** MESSANGER magnetic field data for the first magnetospheric transit on day 181 of 2011 from just after the inbound magnetopause crossing to just before the outbound magnetopause crossing [cf. Winslow *et al.*, 2013]. Top panel shows magnetic field data in Cartesian MSO coordinates:  $B_X$  (red),  $B_Y$  (green), and  $B_Z$  (blue); the total field magnitude,  $B_T$  (black) and the negative of  $B_T$  (grey); and spacecraft planetocentric distance in  $R_M$  (dashed curve, right-hand scale). Middle panel shows the total power spectral density from 0.05 to 10 Hz computed from differenced 20 samples/s data. Bottom panel shows the magnetic field from which the internal planetary offset dipole field has been subtracted in the same coordinates as the top panel, but where the black and gray traces show the magnitude of the residual field and its negative.

[16] The  $\sigma_{2X}$ ,  $\sigma_{2Y}$ , and  $\sigma_{2Z}$  values are the 20-s running standard deviations of  $\delta B_{2X}$ ,  $\delta B_{2Y}$ , and  $\delta B_{2Z}$ , respectively.

[17] To filter periods above 300 s, we chose a three-pass box-car average applied to the 1-s averaged data with 75, 105, and 135 points, respectively yielding 50% attenuation at 293 s period. The average is denoted  $\langle \delta \mathbf{B} \rangle_{300}$  and the passband for 20 to 300 s is calculated as

$$\delta \mathbf{B}_3 = \langle \delta \mathbf{B} \rangle_{20} - \langle \delta \mathbf{B} \rangle_{300} \quad (5)$$

[18] The  $\sigma_{3X}$ ,  $\sigma_{3Y}$ , and  $\sigma_{3Z}$  are the running standard deviations of  $\delta B_{3X}$ ,  $\delta B_{3Y}$ , and  $\delta B_{3Z}$ .

[19] Results for  $\delta \mathbf{B}_2$ ,  $\delta \mathbf{B}_3$ ,  $\sigma_1$ ,  $\sigma_2$ , and  $\sigma_3$  are shown in Figure 5 for the examples. Because  $\sigma_2$  and  $\sigma_3$  are running standard deviations, they can be exceeded by the values of  $\delta \mathbf{B}_2$  or  $\delta \mathbf{B}_3$ . Differences between the two passes are reflected in  $\delta \mathbf{B}_2$ ,  $\delta \mathbf{B}_3$ ,  $\sigma_2$ , and  $\sigma_3$ . The  $\delta \mathbf{B}_2$  and  $\delta \mathbf{B}_3$  values on day 181 often exceeded

10 nT but were lower for the pass on day 186. The  $\sigma_2$  and  $\sigma_3$  values track the perturbations. Even during periods of lower fluctuations on the first pass, the  $\sigma_N$  values were a factor of 3 to 10 greater than those on the second pass. For the second pass, the southern tail lobe was quiet, and fluctuation levels rose on approach to the outbound magnetopause. For the first pass, the tail lobe fluctuations were higher and there was no clear increase near the outbound magnetopause. On both passes, fluctuations were enhanced just inside the magnetopause on the inbound portion of the pass and were generally low through periapsis but were enhanced in the vicinity of the neutral-sheet crossings.

## 4. Disturbance Indices

### 4.1. Average Fluctuations

[20] We calculated time series of the  $\sigma_N$  values for every magnetosphere pass from 2011 day 82 through

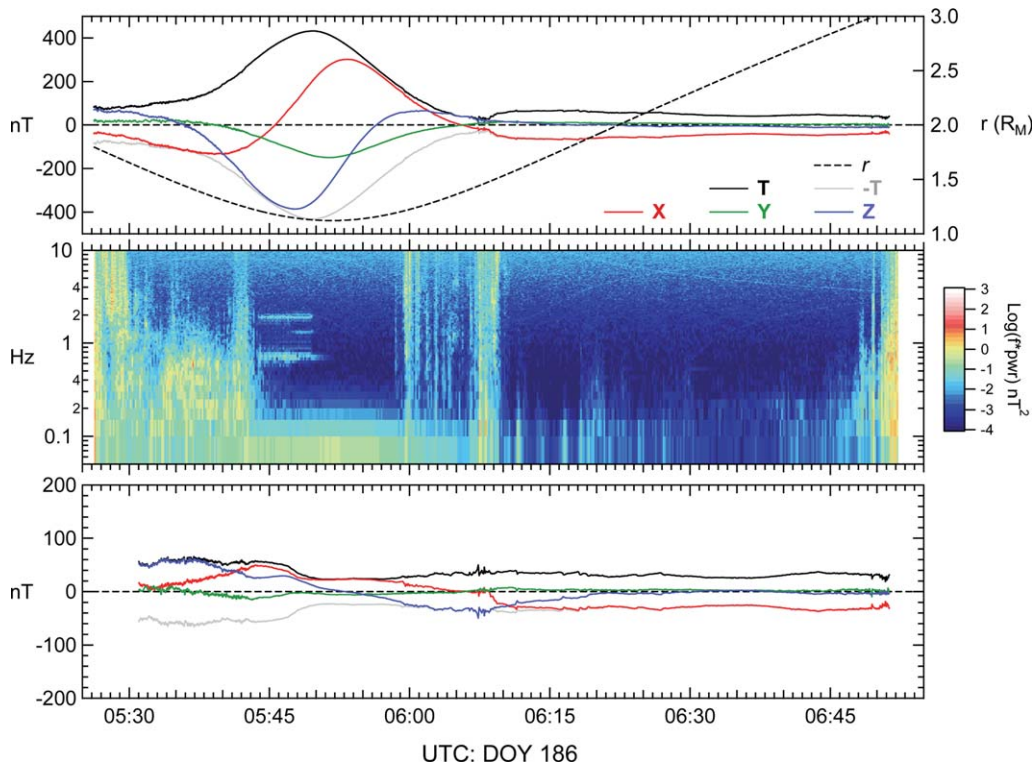


**Figure 3.** Magnetic field data for the first magnetospheric transit on day 186 of 2011 in the same format as in Figure 2.

2012 day 106. Data were separated into ascending and descending orbit segments and then sorted into bins in MSM latitude ( $\lambda$ ) and local time ( $h$ ) with  $\Delta\lambda = 3^\circ$  and  $\Delta h = 1$  h. For each orbit, the averages of  $\sigma_N$  and  $\log_{10}(\sigma_N)$  were calculated in the  $\lambda$ - $h$  bins traversed by that orbit. The average over all orbits was computed for each  $\lambda$ - $h$  bin. For the dates considered, the orbit swept out a figure of revolution about the  $Z$  axis [cf. Figure 1 and *Slavin et al.*, 2007] so that the ascending and descending orbit segments correspond to surfaces with different mean radial distances at a given  $\lambda$  and  $h$ . By treating the data from ascending and descending orbit segments separately, the averages in each  $\lambda$ - $h$  bin correspond only to the radial distance for that orbit segment. The averaged  $\log(\sigma_N)$  versus  $\lambda$  and  $h$  for the ascending and descending orbit segments are shown in Figure 6. The averages, arithmetic means, and relevant standard deviations of these distributions are given in Table 2.

[21] Several features are evident in the  $\log(\sigma_N)$  distributions. The fluctuation levels are higher in the longer-period band:  $\langle\sigma_2\rangle/\langle\sigma_1\rangle \sim 2$  and  $\langle\sigma_3\rangle/\langle\sigma_2\rangle \sim 3$ . The lowest fluctuations occur on the nightside north of  $20^\circ\text{N}$  and south of  $20^\circ\text{S}$  between the equator and the magnetopause. Fluctuations are enhanced near the equator on the nightside and over

the dayside from the equator to  $80^\circ\text{N}$ . There is a localized intensification near  $70^\circ\text{N}$  at noon, most evident in  $\sigma_1$  and  $\sigma_2$ , corresponding to the magnetospheric cusp [*Winslow et al.*, 2012]. There is a local-time asymmetry, opposite for ascending and descending orbit segments. For the ascending data, the fluctuations are stronger at dusk than at dawn,

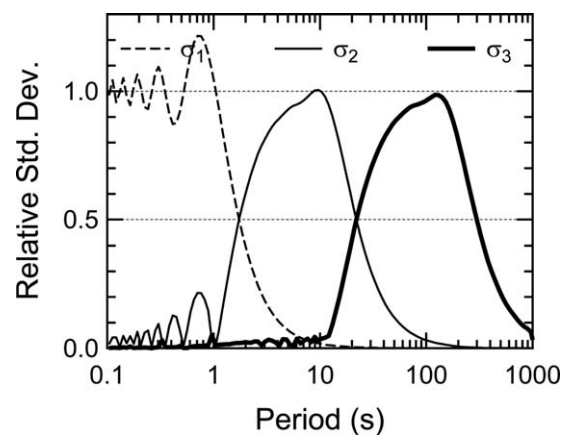


**Figure 4.** Frequency response of filters for magnetic disturbance statistics. Curves show the amplitude of the filtered signal relative to the input signal averaged over all phases.

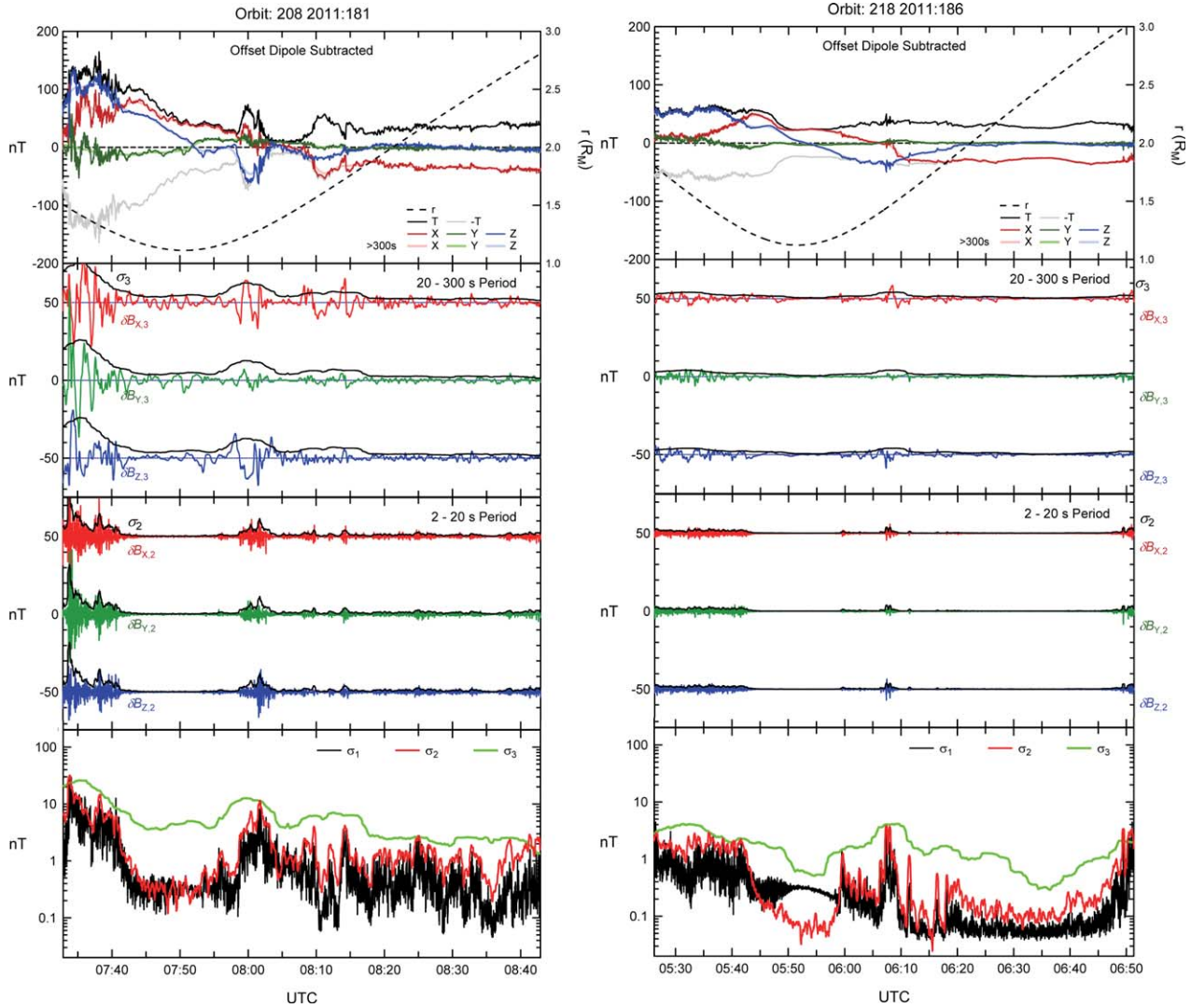


**Figure 5.** Magnetic residuals for the first magnetosphere transit on 2011 day 181 (left) and day 186 (right). Top panels show the residuals in MSO coordinates after subtracting the internal (offset dipole) field (thin darker traces) together with data filtered to remove periods shorter than 300 s (thick light traces);  $\delta B_X$  is in red,  $\delta B_Y$  in green, and  $\delta B_Z$  in blue. The second panels from the top show the residuals in the 20 s to 300 s band,  $\delta B_X$ ,  $\delta B_Y$ , and  $\delta B_Z$ , using the same color coding, together with the 300-s running total standard deviation,  $\sigma_3$ , of these data in black. The third panels from the top show the residuals in the 2 s to 20 s band,  $\delta B_X$ ,  $\delta B_Y$ , and  $\delta B_Z$ , using the same color coding, together with the 300-s running total standard deviation,  $\sigma_2$ , of these data. The bottom panels show  $\sigma_1$ ,  $\sigma_2$ , and  $\sigma_3$  on a log scale in black, red, and green, respectively.

whereas the reverse holds for the descending data. We attribute this asymmetry to the fixed phasing between orbit local time and Mercury heliocentric distance. MESSENGER orbit insertion occurred at Mercury perihelion into a dawn-dusk orbit with periapsis at dawn. Thus, Mercury was closest to the Sun when the spacecraft ascending orbit node was at dusk and the descending orbit node was at dawn. Higher fluctuations correspond to perihelion because the solar wind density and IMF magnitude are on average higher by approximately a factor of 2 than they are at aphelion.

## 4.2. Statistical Distributions and Orbit Averages

[22] We examined the distributions of the  $\sigma_N$  and  $\log(\sigma_N)$  relative to their means in each  $\lambda$ - $h$  bin. The arithmetic distributions are non-Gaussian with maxima below the mean, as expected since the  $\sigma_N$  are positive definite. The  $\log(\sigma_N)$  distributions are Gaussian, however, and we chose to calculate the orbit-averaged fluctuation level,  $d_N$ , from the  $\log(\sigma_N)$ . Labeling  $\lambda$  and  $h$  bins by indices  $l$  and  $m$ , respectively, each pass by  $p$ , and denoting the

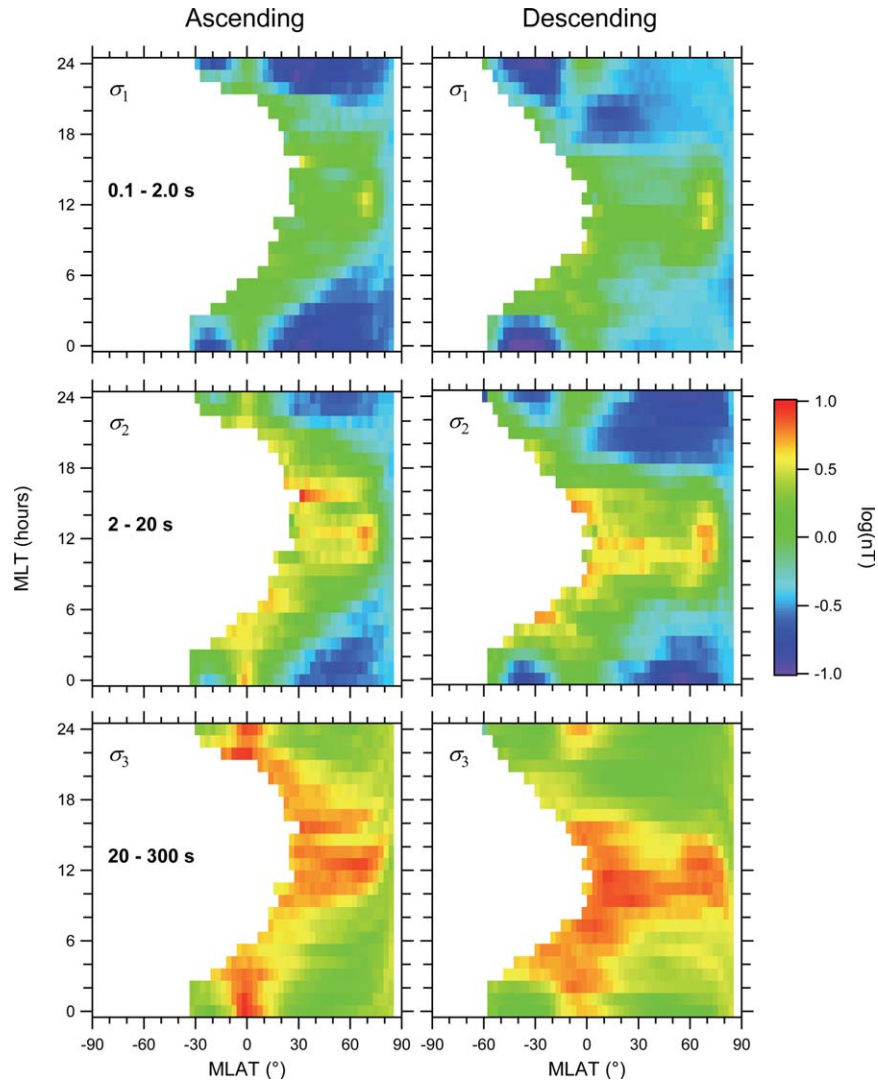


**Figure 6.** Average fluctuation standard deviations versus aberrated local time and magnetic latitude evaluated over 2011 day 082 through 2012 day 107, spanning the entire interval of magnetic field observations while the MESSENGER spacecraft was in a 12 h orbit about Mercury. Bins with transits from fewer than six orbits were left white to show the regions in the south where the MESSENGER orbit did not sample the magnetosphere (cf. Figure 1) as well as the small latitude range poleward of the orbit's maximum northern latitude.

average within each bin for ascending and descending orbit segments by  $\langle \rangle_a$  and  $\langle \rangle_d$ , the disturbance level,  $d_N$ , for the orbit was calculated from

$$d_{N,p} = \frac{1}{n_{p,a} + n_{p,d}} \left( \sum_{l,m} \langle \log(\sigma_{N,l,m,p}) \rangle_a + \sum_{l,m} \langle \log(\sigma_{N,l,m,p}) \rangle_d \right) \quad (6)$$

[23] The summation is over the bins crossed by the orbit, and  $n_{p,a}$  and  $n_{p,d}$  are the total number of bins sampled on the ascending and descending orbit segments, respectively. Subsequently, we use the

subscript  $p$  only when necessary for clarity. The  $d_N$  were ranked from 0% to 100%, denoted  $r_N$ . To combine the  $d_N$  in a single disturbance rank, the average,  $\text{avg}(d_N)$ , and standard deviation,  $\text{dev}(d_N)$ , over all passes were calculated, and the combined disturbance level, denoted  $s_D$ , was computed from

$$s_{D,p} = \frac{1}{3} \sum_{N=1,2,3} \{d_{N,p} - \text{avg}(d_N)\} / \text{dev}(d_N) \quad (7)$$

[24] Dividing by  $\text{dev}(d_N)$  ensures that the period bands contribute equally to  $s_D$  even if their spread



**Table 2.** Magnetic Fluctuation Levels in Mercury’s Magnetosphere Averaged Over MESSENGER’s Orbit<sup>a</sup>

Period Band (s)	Orbit Segment	Average Log [log(nT)]	Geometric Mean (nT) <sup>b</sup>	Arithmetic Mean (nT)
1: 0.1–2	Ascending	$-0.251 \pm 0.33^c$	0.56 ( $\times 2.2$ )	$0.96 \pm 0.74$
	Descending	$-0.235 \pm 0.29$	0.58 ( $\times 1.9$ )	$0.91 \pm 0.73$
	Combined	$-0.242 \pm 0.31$	0.57 ( $\times 2.0$ )	$0.93 \pm 0.73$
2: 2–20	Ascending	$0.057 \pm 0.41$	1.14 ( $\times 2.6$ )	$2.12 \pm 1.65$
	Descending	$-0.064 \pm 0.45$	0.86 ( $\times 2.8$ )	$1.81 \pm 1.60$
	Combined	$-0.013 \pm 0.43$	0.97 ( $\times 2.7$ )	$1.94 \pm 1.63$
3: 20–300	Ascending	$0.518 \pm 0.19$	3.30 ( $\times 1.6$ )	$4.08 \pm 1.75$
	Descending	$0.478 \pm 0.22$	3.00 ( $\times 1.7$ )	$3.81 \pm 1.85$
	Combined	$0.495 \pm 0.21$	3.13 ( $\times 1.6$ )	$3.93 \pm 1.81$

<sup>a</sup>Statistics correspond to the distributions of Figure 6.

<sup>b</sup>Values are the antilog of the mean  $\log(\sigma_N)$ . Parentheses enclose the factor by which the geometric mean is divided or multiplied; that factor corresponds to the standard deviation in the  $\log(\sigma_N)$ .

<sup>c</sup>Listed uncertainties for the average log and arithmetic mean are one standard deviation of the population rather than the standard error in the mean.

in  $d_N$  differs. A combined percentile disturbance rank was derived from the  $s_D$ , denoted  $r_D$ . All of the quantities  $d_N$ ,  $r_N$ ,  $s_D$ , and  $r_D$  retain the variation with local time.

### 4.3. Normalized Disturbance Index

[25] We next consider a measure of disturbance that is independent of Mercury heliocentric distance. We normalized the  $\log(\sigma_{N,lm,p})$  of each orbit to the entire population by taking the difference between  $\log(\sigma_{N,lm,p})$  and the value averaged over all orbits in the same  $\lambda$ - $h$  bin. That is

$$S_{N,p} = \frac{1}{n_{p,a} + n_{p,d}} \left( \sum_{l,m} \langle \log(\sigma_{N,lm,p}/\sigma_{N,lm}) \rangle_a + \sum_{l,m} \langle \log(\sigma_{N,lm,p}/\sigma_{N,lm}) \rangle_d \right) \quad (8)$$

so that  $S_N$  is the log of the geometric mean of  $\sigma_{N,lm,p}/\sigma_{N,lm}$  for the orbit. To convert  $S_N$  to a disturbance measure with physical units, we added the combined average  $\log(\sigma_N)$  from Table 2, denoted as  $\langle \log(\sigma_{N,lm}) \rangle_{a,d}$ , to the  $S_N$ :

$$D_N = S_N + \langle \log(\sigma_{N,lm}) \rangle_{a,d} \quad (9)$$

[26] The antilog of  $D_N$  gives the normalized geometric mean magnetic fluctuation for each pass. We then combined the disturbance measures from the three period bands into a single parameter. The widths of the  $S_N$  distributions are not the same, so we computed the standard deviation of each population,  $\text{dev}(S_N)$ , and computed the integrated disturbance index  $S_{D,p}$  as

$$S_{D,p} = \frac{1}{3} \sum_{N=1,2,3} \{S_{N,p} - \text{avg}(S_N)\} / \text{dev}(S_N) \quad (10)$$

where  $\text{avg}(S_N)$  is the average over all passes. Because the mean disturbance values for each pe-

riod range differ,  $S_D$  does not scale to a physical quantity. As with the quantities  $d_N$  and  $s_D$ , ranked indices were computed from the  $S_N$  and  $S_D$  values to give the percentile rank of each pass, denoted by  $R_N$  and  $R_D$ . The  $d_N$ ,  $r_N$ ,  $s_D$ ,  $S_N$ ,  $S_D$ ,  $R_N$ , and  $R_D$  values from day 82 of 2011 through day 106 of 2012 are included in Supporting Information Table 1<sup>1</sup>.

[27] To assess the sensitivity of the results to the period band ranges, we evaluated linear regression coefficients,  $P_r$ , between indices derived from different period bands. The results are given in Table 3. Indices in adjacent period bands are highly correlated, with  $P_r > 0.7$ , whereas bands 1 and 3 are less well-correlated, with  $0.6 < P_r < 0.7$ . Adjacent bands for the normalized indices have higher correlation,  $P_r > 0.79$ , than the unnormalized indices,  $P_r < 0.8$ . The high correlations between adjacent bands imply that the results are insensitive to the choice of the bounding periods. The correlation between bands 1 and 3, for which there is no frequency overlap and within which we expect that fluctuations are due to different physical

**Table 3.** Linear Regression Coefficients,  $P_r$ , between Fluctuation Indices Evaluated Over Different Period Bands

Index	Bands 1 and 2	Bands 2 and 3	Bands 1 and 3
$d_N^a$	0.736	0.796	0.629
$r_N$	0.706	0.783	0.616
avg $r_N$ , $d_N$	0.721	0.790	0.623
$D_N$	0.833	0.842	0.668
$R_N$	0.798	0.838	0.640
avg $D_N$ , $R_N$	0.812	0.840	0.654

<sup>a</sup>See equations (6) and (9) for definitions of  $d_N$  and  $D_N$ . As discussed in text, the quantities  $r_N$  and  $R_N$  are the population rankings of the  $d_N$  and  $D_N$ , respectively.

<sup>1</sup>Additional supporting information may be found in the online version of this article.

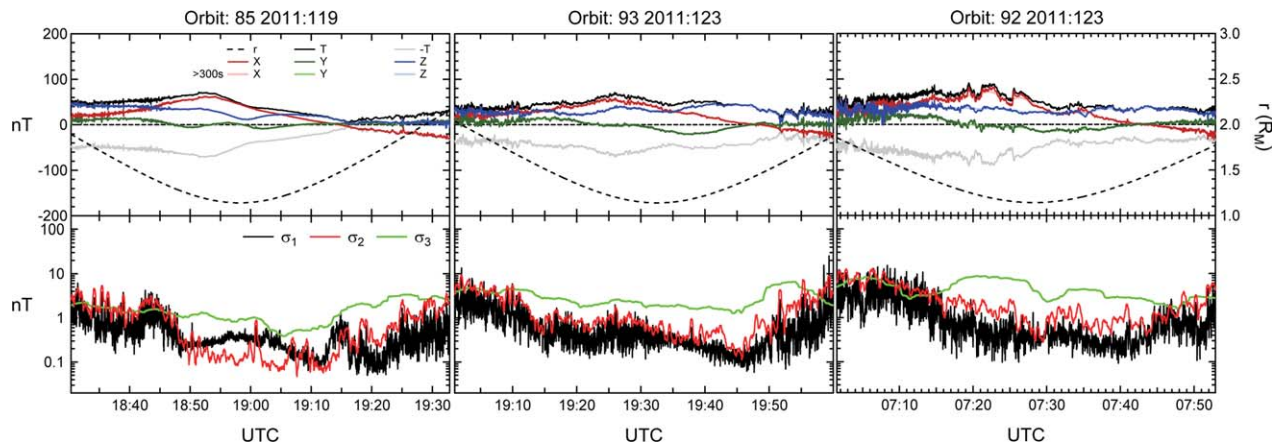


**Figure 7.** Three representative orbits for a near dawn-dusk orbit geometry for extremely quiet (left,  $R_D = 4\%$ ), moderately disturbed (center,  $R_D = 52\%$ ), and highly disturbed (right,  $R_D = 97\%$ ) conditions. The format for each pass is the same as that for the top and bottom panels of Figure 5.

mechanisms (cf. Table 1), implies that at least some of the processes generating the shorter (0.1 to 2 s) and longer (20 s to 300 s) magnetic field fluctuations occur under similar conditions.

#### 4.4. Assessment of Ranked Examples

[28] To illustrate the residuals and  $\sigma_N$  associated with different rankings, Figure 7 shows data from three orbits with approximately dawn-dusk orbit geometry and Figure 8 shows data from three passes with noon-midnight orbit geometry and ascending nodes on the nightside. The rankings for these passes and those shown above are given in Table 4. The ranked order agrees with the qualitative impression of the residuals and with the  $\sigma_N$  levels.

## 5. Summary

[29] We developed a disturbance measure for Mercury's magnetospheric magnetic field using standard deviations of the field in three period bands (0.1–2 s, 2–20 s, and 20–300 s). Orbit averages and a composite index that equally weights the signals in all three passbands were derived. We presented a set of indices that normalizes for the dependence of the fluctuations on local time. The indices provide a quantitative measure to select quiet orbits for studies of the internal planetary magnetic field or to identify orbits exhibiting different levels of activity for magnetospheric studies.

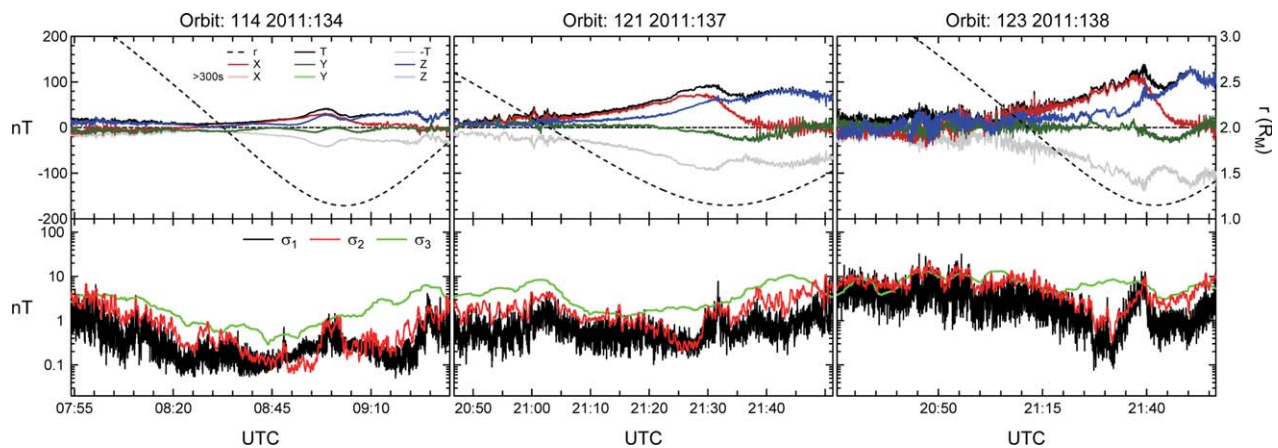


**Figure 8.** Three representative orbits for a near noon-midnight orbit geometry with periapsis on the dayside (cf. Figure 1), for extremely quiet (left,  $R_D = 0.1\%$ ), moderately disturbed (center,  $R_D = 49\%$ ), and highly disturbed (right,  $R_D = 98\%$ ) conditions. The format for each pass is the same as for the top and bottom panels of Figure 5.



**Table 4.** Magnetic Disturbance Values for Selected MESSENGER Orbits

Figure	Orbit Number <sup>a</sup>	Periapsis UTC year:DOY:hhmm	$R_1$ [ $r_1$ ] (%)	$R_2$ [ $r_2$ ] (%)	$R_3$ [ $r_3$ ] (%)	$R_D$ [ $r_D$ ] (%)
3, 5	217	2011:186:0552	28[18]	50[21]	61[49]	46[26]
2, 5	208	2011:181:0751	88[78]	96[74]	99[96]	97[89]
9	85	2011:119:1859	18[10]	6[5]	2[0.3]	4[1.2]
9	93	2011:123:1933	35[31]	60[58]	58[35]	52[40]
9	92	2011:123:0728	90[78]	97[91]	98[87]	97[89]
10	114	2011:134:0903	0.3[0.7]	0.1[6]	0.3[1.0]	0.1[0.8]
10	121	2011:137:2134	57[75]	50[82]	45[58]	49[74]
10	123	2011:138:2143	98[99]	97[93]	94[97]	98[99]

<sup>a</sup>Entries are ordered by the relevant figure number in which the fluctuation measures are shown and then by increasing normalized disturbance rank,  $R_D$ . DOY is day of the year.

## Acknowledgments

[30] The MESSENGER project is supported by the NASA Discovery Program under contracts NAS5-97271 to The Johns Hopkins University Applied Physics Laboratory and NASW-00002 to the Carnegie Institution of Washington. CLJ acknowledges support from MESSENGER Participating Scientist grant NNX11AB84G and from the Natural Sciences and Engineering Research Council of Canada.

## References

Anderson, B. J., M. H. Acuña, D. A. Lohr, J. Scheifele, A. Raval, H. Korth, and J. A. Slavin (2007), The Magnetometer instrument on MESSENGER, *Space Sci. Rev.*, *131*, 417–450, doi:10.1007/s11214-007-9246-7.

Anderson, B. J., M. H. Acuña, H. Korth, M. E. Purucker, C. L. Johnson, J. A. Slavin, S. C. Solomon, and R. L. McNutt Jr. (2008), The magnetic field of Mercury: New constraints on structure from MESSENGER, *Science*, *321*, 82–85.

Anderson, B. J., et al. (2010), The magnetic field of Mercury, *Space Sci. Rev.*, *152*, 307–339, doi:10.1007/s11214-009-9544-3.

Anderson, B. J., C. L. Johnson, H. Korth, M. E. Purucker, R. M. Winslow, J. A. Slavin, S. C. Solomon, R. L. McNutt Jr., J. M. Raines, and T. H. Zurbuchen (2011), The global magnetic field of Mercury from MESSENGER orbital observations, *Science*, *333*, 1859–1862, doi:10.1126/science.1211001.

Anderson, B. J., C. L. Johnson, H. Korth, R. M. Winslow, J. E. Borovsky, M. E. Purucker, J. A. Slavin, S. C. Solomin, M. T. Zuber, and R. L. McNutt Jr. (2012), Low-degree structure in Mercury's planetary magnetic field, *J. Geophys. Res.*, *117*, E00L12, doi:10.1029/2012JE004159.

Bloomfield, P. (2000), *Fourier Analysis of Time Series: An Introduction*, 254 pp., John Wiley, New York.

Boardsen, S. A., B. J. Anderson, M. H. Acuña, J. A. Slavin, H. Korth, and S. C. Solomon (2009), Narrow-band ultra-low-frequency wave observations by MESSENGER during its January 2008 flyby through Mercury's magnetosphere, *Geophys. Res. Lett.*, *36*, L01104, doi:10.1029/2008GL036034.

Boardsen, S. A., T. Sundberg, J. A. Slavin, B. J. Anderson, H. Korth, S. C. Solomon, and L. G. Blomberg (2010), Observations of Kelvin-Helmholtz waves along the dusk-side boundary of Mercury's magnetosphere during MESSENGER's third flyby, *Geophys. Res. Lett.*, *37*, L12101, doi:10.1029/2010GL043606.

Boardsen, S. A., J. A. Slavin, B. J. Anderson, H. Korth, D. Schriver, and S. C. Solomon (2012), Survey of coherent ~1 Hz waves in Mercury's inner magnetosphere, *J. Geophys. Res.*, *117*, A00M05, doi:10.1029/2012JA017822.

Christensen, U. R. (2006), A deep dynamo generating Mercury's magnetic field, *Nature*, *444*, 1056–1058, doi:10.1038/nature05342.

Christensen, U. R., and J. Wicht (2008), Models of magnetic field generation in partly stable planetary cores: Applications to Mercury and Saturn, *Icarus*, *196*, 16–34, doi:10.1016/j.icarus.2008.02.013.

Colombo, G. (1965), Rotational period of the planet Mercury, *Nature*, *208*, 575.

Connerney, J. E. P., and N. F. Ness (1988), Mercury's magnetic field and interior, in *Mercury*, edited by F. Vilas, C. R. Chapman, and M. S. Matthews, pp. 494–513, Univ. of Ariz. Press, Tucson, Ariz.

DiBraccio, G. A., J. A. Slavin, S. A. Boardsen, B. J. Anderson, H. Korth, T. H. Zurbuchen, J. M. Raines, D. N. Baker, R. L. McNutt Jr., and S. C. Solomon (2013), MESSENGER observations of magnetopause structure and dynamics at Mercury, *J. Geophys. Res. Space Phys.*, *118*, 997–1008, doi:10.1002/jgra50123.

Glassmeier, K.-H. (1997), The Hermean magnetosphere and its I-M coupling, *Planet. Space Sci.*, *45*, 119–125.

Glassmeier, K.-H., N. P. Mager, and D. Y. Klimushkin (2003), Concerning ULF pulsations in Mercury's magnetosphere, *Geophys. Res. Lett.*, *30*(18), 1928, doi:10.1029/2003GL017175.

Ip, W.-H. (1987), Dynamics of electrons and heavy ions in Mercury's magnetosphere, *Icarus*, *71*, 441–447.

Jackson, D. J., and D. B. Beard (1977), The magnetic field of Mercury, *J. Geophys. Res.*, *82*, 2828–2836.

Johnson, C. L., et al. (2012), MESSENGER observations of Mercury's magnetic field structure, *J. Geophys. Res.*, *117*, E00L14, doi:10.1029/2012JE004217.

Korth, H., B. J. Anderson, M. H. Acuña, J. A. Slavin, N. A. Tsyganenko, S. C. Solomon, and R. L. McNutt Jr. (2004), Determination of the properties of Mercury's magnetic field by the MESSENGER mission, *Planet. Space Sci.*, *54*, 733–746.

Korth, H., B. J. Anderson, J. M. Raines, J. A. Slavin, T. H. Zurbuchen, C. L. Johnson, M. E. Purucker, R. M. Winslow, S. C. Solomon, and R. L. McNutt Jr. (2011), Plasma pressure in Mercury's equatorial magnetosphere derived from MESSENGER Magnetometer observations, *Geophys. Res. Lett.*, *38*, L22201, doi:10.1029/2011GL049451.

Korth, H., B. J. Anderson, C. L. Johnson, R. M. Winslow, J. A. Slavin, M. E. Purucker, S. C. Solomon, and R. L. McNutt Jr. (2012), Characteristics of the plasma distribution in



- Mercury's equatorial magnetosphere derived from MESSENGER Magnetometer observations, *J. Geophys. Res.*, *117*, A00M07, doi:10.1029/2012JA018052.
- Manglik, A., J. Wicht, and U. R. Christensen (2010), A dynamo model with double diffusive convection for Mercury's core, *Earth Planet. Sci. Lett.*, *289*, 619–628, doi:10.1016/j.epsl.2009.12.007.
- Mayaud, P. N. (1980), *Derivation, Meaning, and Use of Geomagnetic Indices*, *Geophys. Monogr. Ser.*, vol. 22, 154 pp., AGU, Washington, D. C.
- McAdams, J. V., R. W. Farquhar, A. H. Taylor, and B. G. Williams (2007), MESSENGER mission design and navigation, *Space Sci. Rev.*, *131*, 219–246, doi:10.1007/s11214-007-9162-x.
- McAdams, J. V., S. C. Solomon, P. D. Bedini, E. J. Finnegan, R. L. McNutt Jr., A. B. Calloway, D. P. Moessner, M. W. Wilson, D. T. Gallagher, C. J. Ercol, and S. H. Flanigan (2012), MESSENGER at Mercury: From orbit insertion to first extended mission, paper presented at the 63rd International Astronautical Congress, paper IAC-12-C1.5.6, 11 pp., 1–5 Oct., Naples, Italy.
- Ness, N. F., K. W. Behannon, R. P. Lepping, Y. C. Whang, and K. H. Schatten (1974), Magnetic field observations near Mercury: Preliminary results from Mariner 10, *Science*, *185*, 151–160.
- Ness, N. F., K. W. Behannon, and R. P. Lepping (1975), The magnetic field of Mercury, *J. Geophys. Res.*, *80*, 2708–2716.
- Pettengill, G. H., and R. B. Dyce (1965), A radar determination of the rotation of the planet Mercury, *Nature*, *206*, 1240.
- Richer, E., R. Modolo, G. M. Chanteur, S. Hess, and F. Leblanc (2012), A global hybrid model for Mercury's interaction with the solar wind: Case study of the dipole representation, *J. Geophys. Res.*, *117*, A10228, doi:10.1029/2012JA017898.
- Russell, C. T. (1989), ULF waves in the Mercury magnetosphere, *Geophys. Res. Lett.*, *16*, 1253–1256.
- Russell, C. T., D. N. Baker, and J. A. Slavin (1988), The magnetosphere of Mercury, in *Mercury*, edited by F. Vilas, C. R. Chapman, and M. S. Matthews, pp. 514–561, Univ. of Ariz. Press, Tucson, Ariz.
- Slavin, J. A., et al. (2007), MESSENGER: Exploring Mercury's magnetosphere, *Space Sci. Rev.*, *131*, 133–160, doi:10.1007/s11214-007-9154-x.
- Slavin, J. A., et al. (2008), Mercury's magnetosphere after MESSENGER's first flyby, *Science*, *321*, 85–89, doi:10.1126/science.1159040.
- Slavin, J. A., et al. (2009), MESSENGER observations of magnetic reconnection in Mercury's magnetosphere, *Science*, *324*, 606–610, doi:10.1126/science.1172011.
- Slavin, J. A., et al. (2010a), MESSENGER observations of large flux transfer events at Mercury, *Geophys. Res. Lett.*, *37*, L02105, doi:10.1029/2009GL041485.
- Slavin, J. A., et al. (2010b), MESSENGER observations of extreme loading and unloading of Mercury's magnetic tail, *Science*, *329*, 665–668, doi:10.1126/science.1188067.
- Slavin, J. A., et al. (2012a), MESSENGER and Mariner 10 flyby observations of magnetotail structure and dynamics at Mercury, *J. Geophys. Res.*, *117*, A01215, doi:10.1029/2011JA016900.
- Slavin, J. A., et al. (2012b), MESSENGER observations of a flux-transfer-event shower at Mercury, *J. Geophys. Res.*, *117*, A00M06, doi:10.1029/2012JA017926.
- Solomon, S. C. (1976), Some aspects of core formation in Mercury, *Icarus*, *28*, 509–521.
- Solomon, S. C., R. L. McNutt Jr., R. E. Gold, and D. L. Domingue (2007), MESSENGER mission overview, *Space Sci. Rev.*, *131*, 3–39, doi:10.1007/s11214-007-9247-6.
- Srnka, L. J. (1976), Magnetic dipole moment of a spherical shell with TRM acquired in a field of internal origin, *Phys. Earth Planet. Inter.*, *11*, 184–190.
- Stanley, S., and A. Mohammadi (2008), Effects of an outer thin stably stratified layer on planetary dynamos, *Phys. Earth Planet. Inter.*, *168*, 179–190, doi:10.1016/j.pepo.2008.06.016.
- Stevenson, D. J. (1982), Reducing the non-axisymmetry of a planetary dynamo and an application to Saturn, *Geophys. Astrophys. Fluid Dyn.*, *21*, 113–127.
- Stevenson, D. J., T. Spohn, and G. Schubert (1983), Magnetism and thermal evolution of the terrestrial planets, *Icarus*, *54*, 466–489.
- Sundberg, T., S. A. Boardsen, J. A. Slavin, L. G. Blomberg, and H. Korth (2010), The Kelvin-Helmholtz instability at Mercury: An assessment, *Planet. Space Sci.*, *58*, 1434–1441, doi:10.1016/j.pss.2010.06.008.
- Sundberg, T., et al. (2012a), MESSENGER observations of dipolarization events in Mercury's magnetotail, *J. Geophys. Res.*, *117*, A00M03, doi:10.1029/2012JA017756.
- Sundberg, T., S. A. Boardsen, J. A. Slavin, B. J. Anderson, H. Korth, T. H. Zurbuchen, J. M. Raines, and S. C. Solomon (2012b), MESSENGER orbital observations of large-amplitude Kelvin-Helmholtz waves at Mercury's magnetopause, *J. Geophys. Res.*, *117*, A04216, doi:10.1029/2011JA017268.
- Trávníček, P. M., P. Hellinger, D. Schriver, D. Herčík, J. A. Slavin, and B. J. Anderson (2009), Kinetic instabilities in Mercury's magnetosphere: Three-dimensional simulation results, *Geophys. Res. Lett.*, *36*, L07104, doi:10.1029/2008GL036630.
- Uno, H., C. L. Johnson, B. J. Anderson, H. Korth, and S. C. Solomon (2009), Mercury's internal magnetic field: Constraints from regularized inversions, *Earth Planet. Sci. Lett.*, *285*, 328–339.
- Winslow, R. M., C. L. Johnson, B. J. Anderson, H. Korth, J. A. Slavin, M. E. Purucker, and S. C. Solomon (2012), Observations of Mercury's northern cusp region with MESSENGER's Magnetometer, *Geophys. Res. Lett.*, *39*, L08112, doi:10.1029/2012GL051472.
- Winslow, R. M., B. J. Anderson, C. L. Johnson, J. A. Slavin, H. Korth, M. E. Purucker, D. N. Baker, and S. C. Solomon (2013), Mercury's magnetopause and bow shock from MESSENGER observations, *J. Geophys. Res. Space Phys.*, *118*, 2213–2227, doi:10.1002/jgra50237.